Bayesian Approaches to Multipath-Enhanced Device-Free Localization

Martin Schmidhammer*, Benjamin Siebler*, Christian Gentner*, Stephan Sand*, Uwe-Carsten Fiebig*
*German Aerospace Center (DLR), Institute of Communications and Navigation, Wessling, Germany
{martin.schmidhammer, benjamin.siebler, christian.gentner, stephan.sand, uwe.fiebig }@dlr.de

***Abstract*—Device-free localization systems infer presence and location of moving users by measuring user-induced perturbations in the signal power between wireless network nodes. Thereby, users not only induce perturbations to the power of the line-of-sight, but also to the power of reflected and scattered signals which are observed in the received signal as multipath components. Since the propagation paths of multipath components differ inherently from the line-of-sight path, these propagation paths can be considered as additional network links. This extended network determines the multipath-enhanced device-free localization system. Based on empirical models that relate perturbations in the power of multipath components to the user location, the localization problem can be solved by nonlinear Bayesian filtering. In this work, we therefore investigate the point mass filter and the particle filter as possible solutions. Using simulations, we demonstrate the applicability of these filter solutions for multipath-enhanced device-free localization. The overall localization performance is comparable for both filters. Further, the simulation results indicate an improvement of the localization performance of multipath-enhanced device-free localization compared to device-free localization.**

***Index Terms*—Sequential Bayesian estimation, device-free localization, extended Kalman filter, particle filter, point mass filter.**

I. Introduction

In today's wireless world, smartphones widely use Bluetooth and WLAN as radio technologies for indoor communication covering short to medium range and low to high data rate communications. The scientific community has extensively studied their suitability for indoor localization and several commercial products exist today to enable indoor localization [1]. According to [2], the global indoor location market will grow from \$6.1 billion in 2020 to \$17 billion by 2025 with the dominant technologies beeing WLAN and Bluetooth. Location dependent measurements range from received signal strength (RSS) to time of flight based round trip time measurements [3]. While many use cases require the precise localization of a persons's device, there exist several use cases that need to localize persons without a device [4]. For instance, home security systems need to detect the presence of intruders who try to avoid detection by not carrying smartphones. Similar, a smart climate control for a room needs to detect the presence and number of occupants to adjust temperature, humidity and ventilation automatically without requiring any user interaction. Further, a surround sound system should track the location of listeners in a room without requiring manual adjustments every time a listener moves within the room. Hence, there is significant commercial interest in WLAN sensing technology enabling device-free localization (DFL).

Current DFL systems infer the presence and location of these non-equipped users by measuring the RSS between network nodes along the line-of-sight (LoS) path. Using empirical propagation models, the DFL system directly relates these RSS measurements to the user location [5], [6], [7]. Thereby, the localization accuracy of such DFL systems improves with the number of network nodes [7]. An increasing number of network nodes, however, results in increasing infrastructural efforts. Motivated by [8], where we have shown that users also induce variations in the power of multipath components (MPCs), we have proposed in [9] a novel multipath-enhanced device-free localization (MDFL) approach, which considers the propagation paths of MPCs as additional network links. For similar underlying networks, MDFL is shown to improve the localization performance compared to DFL and helps to reduce infrastructural requirements. In this paper we present corresponding nonlinear Bayesian filter solutions for the MDFL approach. Based on simulations we evaluate the applicability of the individual filters. Moreover, we apply the filter solutions for both DFL and MDFL, which allows to compare the performance of the two systems.

II. Multipath-enhanced Device-free Localization

A. Network and Propagation Model

An MDFL system relies on a network of N_{Tx} transmitting and N_{Rx} receiving nodes, which can be collocated or individually placed. In this work we consider $N_{\mathrm{Tx}} = N_{\mathrm{Rx}} = N$ collocated transmitting and receiving nodes at known locations $\{\boldsymbol{r}_{\mathrm{TR}_1}, \ldots, \boldsymbol{r}_{\mathrm{TR}_\mathrm{N}}\}$. Thereby, a network link l is determined by network nodes $\boldsymbol{r}_{\mathrm{TR_i}}$ and $\boldsymbol{r}_{\mathrm{TR_j}}$, where $i, j \in \{1, \ldots, N\}$ and $i \neq j$. For each link, the received signal is modeled as a superposition of scaled and delayed replica of a known transmit signal [10]. Due to reflections off the surrounding environment, these comprise the LoS component and a finite number of N_l MPCs, which can be expressed as

$$y_l(t) = \sum_{n=1}^{N_l} \alpha_{l,n}(t) s_l(t - \tau_{l,n}) + n_l(t). \tag{1}$$

The variables $\alpha_{l,n}$(t) and $\tau_{l,n}$ denote the time-variant, complex amplitude and the static propagation delay of the n-th component and $n_l(t)$ denotes white circular symmetric normal distributed noise with variance $\sigma^2_{y_l}$. For notational

convenience, LoS components are considered as MPCs in the remainder of this paper. An exemplary signal propagation for a single network link is highlighted in Fig. 1, including LoS and MPCs due to first order reflections from surrounding walls.

The idea of MDFL is to use variations in the power of MPCs for DFL. In order to extract location information from variations in the power of MPCs, we need to model the corresponding propagation paths. In [9], we have therefore introduced reflection sequences that describe the signal propagation for each MPC from transmitting to receiving node, chronologically. Thereby, the surrounding environment is represented by a finite number of reflecting surfaces, which determine the set $\mathcal{S}$. Using tuple notation, the propagation path corresponding to MPC n of link l is thus expressed by the sequence $\xi_{l,n} = (s_b)$ with $s_b \in \mathcal{S}$. Note that the length of the sequence, denoted by $N_{\xi_{l,n}}$, is determined by the order of reflection. Following [11] and [12], we can subsequently construct virtual nodes, i.e., virtual transmitters (VTs) and virtual receivers (VRs), by mirroring the physical nodes according to the reflection sequences. Thus, the resulting locations of the virtual nodes for sequence $\xi_{l,n}$ are denoted by $\boldsymbol{r}^{(u)}_{\mathrm{VT}_{l,n}}$ and $\boldsymbol{r}^{(N_{\xi_{l,n}}-u)}_{\mathrm{VR}_{l,n}}$, where the index $u \in \{0, \dots, N_{\xi_{l,n}}\}$ is referring to equidistant (virtual) node pairs. The distances between these node pairs correspond to the length of the physical propagation path, and thus, to the delay of the MPC. For any node pair, i.e. irrespective of index u, the length of the propagation path can be expressed as

$$d\left(\xi_{l,n}\right) = d_{l,n} = \|\boldsymbol{r}^{(u)}_{\mathrm{VT}_{l,n}} - \boldsymbol{r}^{(N_{\xi_{l,n}}-u)}_{\mathrm{VR}_{l,n}}\|, \tag{2}$$

where $\boldsymbol{r}^{(0)}_{\mathrm{VT}_{l,n}}$ and $\boldsymbol{r}^{(0)}_{\mathrm{VR}_{l,n}}$ refer to the physical transmitting and receiving nodes. Since the intersection points between the paths of related node pairs correspond to the physical reflection points, we can finally reconstruct the physical propagation paths geometrically similar to optical ray-tracing [11].

In this work, we assume that all observable MPCs of the received signal modeled in (1) are perfectly associated. That means, the MPCs of link l are represented by the reflection sequences $\xi_{l,n} \in \mathcal{X}^\star_l$, where $\mathcal{X}^\star_l$ denotes the set of associated sequences. Combining the associated sequences for the whole network results in the union set $\mathcal{X}^\star = \cup_l \mathcal{X}^\star_l$. Eventually, the cardinality $|\mathcal{X}^\star| = \sum_l N_l$ determines the amount of all MPCs used for MDFL.

B. Measurement Model

During the online localization phase, the MDFL system continuously measures the variations in the power of all associated MPCs. Therefore, the amplitude values are estimated for each MPC at time instant k and the measured power can be calculated. Normalizing the measured power to the power of the idle channel which was determined during the initialization period yields the power variations of MPCs. Thus, the measurement vector $\mathbf{z}_k \in \mathbb{R}^{|\mathcal{X}^\star|}$ can be composed by stacking the measured power changes for all links as

$$\mathbf{z}_k = \left[\dots, \mathrm{z}_{l,n}(k), \dots\right]^{\mathrm{T}}, \quad \forall l, n : \xi_{l,n} \in \mathcal{X}^\star, \tag{3}$$

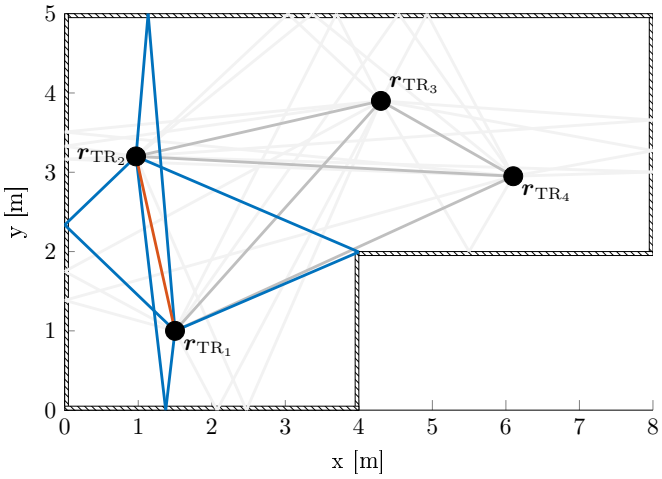

Fig. 1: Exemplary MDFL network of four network nodes at locations $\boldsymbol{r}_{\mathrm{TR}_i}$, $i = \{1, 2, 3, 4\}$. Reflecting surfaces of the surrounding environment are given by hatched lines. For the network link between $\boldsymbol{r}_{\mathrm{TR}_1}$ and $\boldsymbol{r}_{\mathrm{TR}_2}$ the multipath propagation is explicitly highlighted: physical propagation paths of LoS and MPCs are red and blue. For the remaining network links the propagation paths are indicated in gray (LoS in dark gray and MPCs in light gray).

with $\mathrm{z}_{l,n}(k)$ defined in dB. Following [8], we simulate the user induced variations in the power of MPCs based on the scalar theory of diffraction (see also Sec. IV-A).

For applying MDFL we require a model that relates the measured changes in the power of MPCs to the user state

$$\mathbf{x}_k = [\mathbf{r}_k^T, \mathbf{v}_k^T]^T, \tag{4}$$

including position $\mathbf{r}_k$ and velocity $\mathbf{v}_k$ of the user, i.e., $\boldsymbol{h}(\mathbf{x}_k)$. Therefore, we model the measurement vector (3) as

$$\mathbf{z}_k = \boldsymbol{h}(\mathbf{x}_k) + \mathbf{w}_k, \tag{5}$$

assuming Gaussian measurement noise $\mathbf{w}_k \sim \mathcal{N}(\mathbf{0}, \boldsymbol{R})$ with covariance matrix $\boldsymbol{R} \in \mathbb{R}^{|\mathcal{X}^\star| \times |\mathcal{X}^\star|}$ defined as

$$\boldsymbol{R} = \mathrm{diag}(\dots, \sigma^2_{l,n}, \dots), \quad \forall l, n : \xi_{l,n} \in \mathcal{X}^\star. \tag{6}$$

Bases on measurements, we have shown in [8] that user induced variations in the power of MPCs can be modeled by superimposing the user impact on each pair of related virtual nodes. Similarly to [9], we approximate this impact on the individual node pairs using the empirical exponential model [6]. Thus, depending on the user location $\boldsymbol{r}_k$, we express changes in the power of an MPC corresponding to sequence $\xi_{l,n}$ in (5) as the sum

$$h_{l,n}(\boldsymbol{x}_k) = \sum_{u=0}^{N_{\xi_{l,n}}} \phi_{l,n} e^{-\delta^{(u)}_{l,n}(\boldsymbol{r}_k)/\kappa_{l,n}}, \tag{7}$$

with the parameter $\phi_{l,n}$ as the maximum modeled power change in dB and $\kappa_{l,n}$ as the decay rate. The excess path length $\delta^{(u)}_{l,n}(\boldsymbol{r}_k)$ of the u-th node pair is calculated by

$$\delta^{(u)}_{l,n}(\boldsymbol{r}_k) = \|\boldsymbol{r}^{(u)}_{\mathrm{VT}_{l,n}} - \boldsymbol{r}_k\| + \|\boldsymbol{r}^{(N_{\xi_{l,n}}-u)}_{\mathrm{VR}_{l,n}} - \boldsymbol{r}_k\| - d_{l,n}, \tag{8}$$

with path length $d_{l,n}$ as defined in (2).

III. Bayesian Localization Approaches

The localization problem described in Sec. II can be formulated using the state-space representation: First, by a measurement model which relates the measured power changes of MPCs to the user state, as given in (5). And second, by a transition model which describes the spatio-temporal evolution of the user state. In literature, a common choice for the transition model is the white noise acceleration model [7], [13]. Therefore, the state equation is

$$\mathbf{x}_k = \mathbf{A}\mathbf{x}_{k-1} + \mathbf{n}_k, \tag{9}$$

with transition matrix $\mathbf{A}$ and zero-mean white Gaussian process noise $\mathbf{n}_k$ with covariance matrix $\mathbf{Q}$. The transition and covariance matrices are expressed as

$$\mathbf{A} = \begin{bmatrix} 1 & 0 & T_g & 0 \\ 0 & 1 & 0 & T_g \\ 0 & 0 & 1 & 0 \\ 0 & 0 & 0 & 1 \end{bmatrix}, \quad \mathbf{Q} = \sigma_p^2 \begin{bmatrix} \frac{T_g^3}{3} & 0 & \frac{T_g^2}{2} & 0 \\ 0 & \frac{T_g^3}{3} & 0 & \frac{T_g^2}{2} \\ \frac{T_g^2}{2} & 0 & T_g & 0 \\ 0 & \frac{T_g^2}{2} & 0 & T_g \end{bmatrix}, \tag{10}$$

where T_g is the time between two adjacent measurements and σ_p^2 is the process noise intensity of physical dimension $\left[\mathrm{m}^2/\mathrm{s}^3\right]$, which needs to be set according to application requirements [13]. Probabilistically, the measurement and transition models can be expressed by the conditional probability density function (PDF) $p(\mathbf{z}_k|\mathbf{x}_k)$ and the transition prior distribution $p(\mathbf{x}_k|\mathbf{x}_{k-1})$, respectively.

The goal of sequential Bayesian estimation is to determine the PDF of the user state $\mathbf{x}_k$ by computing the posterior density $p(\mathbf{x}_k|\mathbf{z}_{1:k})$ applying the general Bayesian update recursion [14]. A possible Bayesian approach for solving the nonlinear system is the extended Kalman filter (EKF). The EKF linearizes the system equations and approximates the posterior density with a Gaussian distribution. However, for the given localization problem the density can hardly be assumed to be Gaussian. Thus, the EKF is likely to be unstable and to diverge (see Sec. IV-B). In the following we therefore present alternative filter solutions which approximate the posterior PDF numerically and are thus more suitable for nonlinear and non-Gaussian processes.

A. Point Mass Filter

The point mass filter (PMF) approximates the posterior distribution with the discrete density

$$p(\mathbf{x}_k|\mathbf{z}_{1:k}) \approx \sum_{i=1}^{N_\mathrm{s}} w_{k|k}^i \delta(\mathbf{x}_k - \mathbf{x}^i), \tag{11}$$

where $\delta(\cdot)$ denotes the Dirac delta function and $\mathbf{x}^i$ represents the i-th grid point of the deterministic grid $\{\mathbf{x}^i\}_{i=1}^{N_\mathrm{s}}$ [14]. The weights $w_{k|k}^i$ are calculated by

$$w_{k|k}^i = \frac{1}{c_k} w_{k|k-1}^i p(\mathbf{z}_k|\mathbf{x}^i), \tag{12}$$

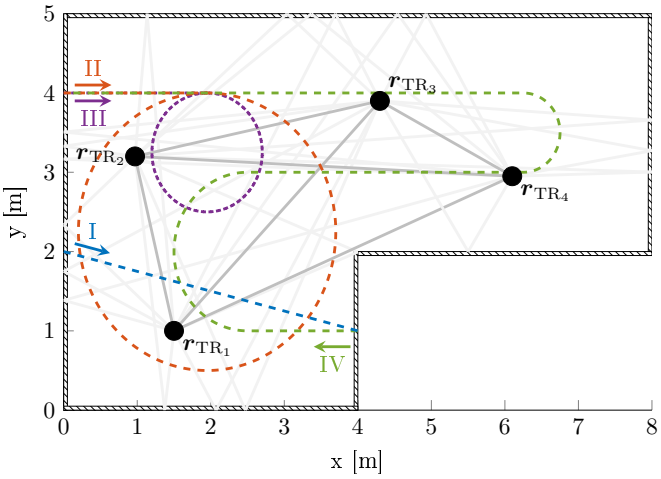

Fig. 2: Simulation trajectories for different runs. Initial moving direction of each trajectory is indicated by colored arrows. Underlying MDFL network is indicated in gray (see Fig. 1).

with normalization $c_k = \sum_{j=1}^{N_\mathrm{s}} w_{k|k-1}^j p(\mathbf{z}_k|\mathbf{x}^j)$ and the likelihood distribution $p(\mathbf{z}_k|\mathbf{x}^i)$. The predicted weights are

$$w_{k|k-1}^i = \sum_{j=1}^{N_\mathrm{s}} w_{k-1|k-1}^j p(\mathbf{x}^i|\mathbf{x}^j). \tag{13}$$

where $p(\mathbf{x}^i|\mathbf{x}^j)$ is the transition prior distribution applied to discretized grid points, which equals a multidimensional convolution [14]. Therewith, the complexity of the PMF grows quadratically with N_s.

B. Particle Filter

Also the particle filter (PF) approximates the posterior distribution with a discrete density

$$p(\mathbf{x}_k|\mathbf{z}_{1:k}) \approx \sum_{i=1}^{N_\mathrm{s}} w_k^i \delta(\mathbf{x}_k - \mathbf{x}_k^i). \tag{14}$$

However, the PDF is approximated using a stochastic grid, i.e., a set of weighted particles $\{\mathbf{x}_k^i\}_{i=1}^{N_\mathrm{s}}$. Following the generic PF, the particles are drawn from an importance density [15]. Commonly this importance density is set equal to the transition prior distribution [14], which simplifies the weight update in the filter to

$$w_k^i = \frac{1}{c_k} w_{k-1}^i p(\mathbf{z}_k|\mathbf{x}_k^i), \tag{15}$$

with normalization $c_k = \sum_{j=1}^{N_\mathrm{s}} w_{k-1}^j p(\mathbf{z}_k|\mathbf{x}_k^j)$ and the likelihood distribution $p(\mathbf{z}_k|\mathbf{x}_k^i)$. Counteracting the problem of degeneracy, the PF applies resampling [15].

IV. Numerical Evaluation

A. Simulation Setup and Evaluation Metric

The localization approaches introduced in Sec. III are evaluated numerically. Therefore, we consider a fully meshed network of $N = 4$ collocated transmitting and receiving nodes. All nodes are located at the same height and correspond to the

Parameter		Value	
		PF	PMF
Particles/grid points	N_s	1000	3331
Grid point spacing	Δ_r	-	$0.1\,\mathrm{m}$
Measurement rate	T_g	$0.01\,\mathrm{s}$	
Process noise intensity	σ_p^2	$0.1\,\mathrm{m}^2/\mathrm{s}^3$	
Measurement noise	$\sigma_{l,n}$	$0.75\,\mathrm{dB}$	
Max. power change (7)	$\phi_{l,n}$	$[-8.91\,\mathrm{dB}, -3.74\,\mathrm{dB}]$	
Decay rate (7)	$\kappa_{l,n}$	$[0.016, 0.072]$	

TABLE I: Filter parameters.

Trajectory	MDFL			DFL		
	EKF	PF	PMF	EKF	PF	PMF
I	1.01*	0.25	0.28	-	1.93	1.82
II	4.72*	0.84	0.62	-	2.43	2.29
III	2.33*	1.08	0.75	-	1.99	1.80
IV	5.41*	0.47	0.41	-	1.08	1.57
overall	3.94*	0.65	0.51	-	1.78	1.87

TABLE II: Mean RMSE [m] for each trajectory and an overall result. *Estimation strongly diverges.

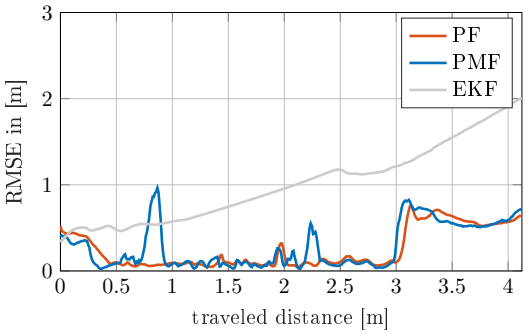

Fig. 3: RMSE results of MDFL for Trajectory I.

height of the body center of the user. The multipath propagation environment is characterized by six reflecting surfaces that may represent a typical office space. The arrangement of the surfaces as well as the arrangement of the network nodes are shown to scale in Fig. 1. Considering only first order reflections, the network consists of six links in LoS and 20 visible links corresponding to MPCs. Accordingly, the measurement vectors of (3) for DFL and MDFL are $\mathbf{z}_k^{\mathrm{DFL}} \in \mathbb{R}^6$ and $\mathbf{z}_k^{\mathrm{MDFL}} \in \mathbb{R}^{26}$. Applying the physical model in [8], we simulate user induced variations in the power of MPCs, i.e., the measurements, for four exemplary trajectories. Thereby, the user is modeled as an elliptical cylinder with major axis of $0.55\,\mathrm{m}$, minor axis of $0.25\,\mathrm{m}$, and a height of $1.8\,\mathrm{m}$. The reader is referred to [8] for further details on the physical model. The trajectories for the simulation are shown in Fig. 2 including starting point and moving direction. Based on the simulated measurements, we apply the PMF and the PF for localization. All parameters used for the filtering approaches are summerized in Table I and are applied for each trajectory. The PF is initialized by uniformly distributing particles in the observation area. Equivalently, the weights of the PMF are initially set equal.

Given the posterior densities of (11) and (14), we can calculate the minimum mean square error (MMSE) estimate of the user state for PMF and PF as the weighted sum

$$\hat{\mathbf{x}}_k^{PMF} = \sum_{i=1}^{N_\mathrm{s}} w_{k|k}^i \mathbf{x}^i \quad \text{and} \quad \hat{\mathbf{x}}_k^{PF} = \sum_{i=1}^{N_\mathrm{s}} w_k^i \mathbf{x}_k^i. \tag{16}$$

For the evaluation of the filter results, we calculate the root mean square error (RMSE) as

$$\mathrm{RMSE}_k = \sqrt{E\left[\|\hat{\boldsymbol{r}}_k - \boldsymbol{r}_k\|^2\right]}, \tag{17}$$

where $\boldsymbol{r}_k$ is the true user location and $\hat{\boldsymbol{r}}_k$ is the respective location estimate of PMF and PF extracted from the user state calculated in (16).

B. Numerical Results

For each trajectory we have evaluated 500 realizations accounting for measurement noise. The presented RMSE results are determined by averaging over these realizations. A summary of the individual filter performances is given in Table II providing the mean RMSE values for each trajectory. In addition to the proposed PMF and PF, we also show the results of an EKF solution (parameter settings similar to Table I). In [7], the EKF is used as benchmark system for DFL, however, we could not obtain reasonable results for DFL and only unstable and diverging results for MDFL, even though the EKF was initialized ideally. The poor performance of the EKF can be explained by the sparse network configuration ($N = 4$ network nodes), which results in a non-Gaussian and often multimodal posterior density. In contrast, both PMF and PF could achieve stable results that significantly outperform the EKF for MDFL (see also Fig. 3).

Fig. 3 shows the RMSE results for Trajectory I using MDFL. Both PMF and PF achieve a sub-meter localization performance over the entire trajectory, which also applies at the beginning of the trajectory. Due to the propagation paths of the MPCs, which are in the proximity of the starting point of Trajectory I (see Fig. 2), the filters immediately obtain a good location estimate. Compared to the PF, the RMSE of the PMF slightly deviates at a traveled distance of $0.8\,\mathrm{m}$ and $2.2\,\mathrm{m}$. This deviation can be explained by local multimodalities of the posterior, which are resolved by the PF due to resampling. After a traveled distance of $3\,\mathrm{m}$ the RMSE increases for both PMF and PF. Due to the network structure, the trajectory lies after this point in a blank area that is not touched by any propagation path and the user does not induce any perturbations. Thus, the estimated posterior spreads over that blank area, here, between $x \in [2.5\,\mathrm{m}, 4\,\mathrm{m}]$ and $y \in [0\,\mathrm{m}, 2\,\mathrm{m}]$.

The starting points of Trajectories II and III are also located in a blank area (see Fig. 2). As shown in the results of the PF in Fig. 4, no user-induced perturbations can be measured initially and thus the PDF spreads over the entire observed area. An accurate position estimate is only obtained when the user induces perturbations in the power of any network link, which is the case for MDFL after $1\,\mathrm{m}$ and for DFL after almost $3\,\mathrm{m}$. In addition to the initial phase, also the

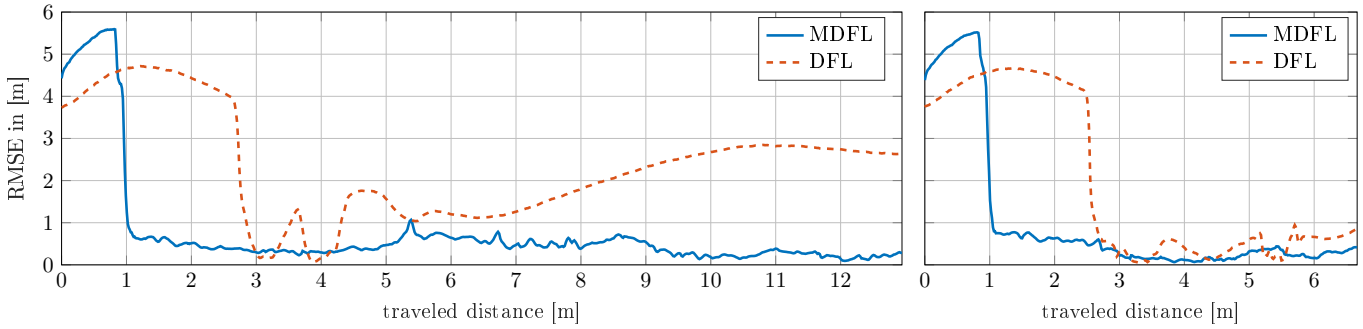

(a) Trajectory II.

(b) Trajectory III.

Fig. 4: RMSE results of DFL and MDFL both applying the PF solution, for Trajectory II and Trajectory III.

comparison of the further course of Trajectories II and III give indication for the spatial localization capabilities of DFL and MDFL. While we obtain a sub-meter localization performance for MDFL almost entirely over both trajectories, the RMSE results for DFL strongly deviate for Trajectory II. The course of Trajectory II is mostly outside the DFL network and thus the user does not impact the signal propagation in LoS. For Trajectory III, also the DFL approach achieves localization performance of less than one meter, but is still outperformed by MDFL on average.

As shown in Fig. 2, Trajectory IV is the longest scenario leading through the whole observation area. On average, the localization performance is therefore only weakly distorted by initialization effects or other local geometric effects. With a mean RMSE of $0.41\,\mathrm{m}$ (PMF) and $0.47\,\mathrm{m}$ (PF), as given in Table II, both filters achieve a very similar localization performance for MDFL. For DFL, the performance of the PMF degrades to $1.57\,\mathrm{m}$ and of the PF to $1.08\,\mathrm{m}$. Therewith, the PF outperforms the PMF in this specific scenario. Due to the very sparse DFL network, the posterior density is more likely to be multimodal. Here, the PF could correctly resolve these multimodalities. Note, however, that if the PF would resolve for the wrong mode, the filter would diverge. The deterministic grid of the PMF completely avoids divergence.

V. Conclusion

In this paper, we have presented the point mass filter (PMF) and the particle filter (PF) as nonlinear Bayesian filter solutions for device-free localization (DFL) and multipath-enhanced device-free localization (MDFL). Based on simulations of a sparse network comprising four collocated transmitting and receiving nodes the filter solutions were evaluated numerically. Overall, we have thereby demonstrated the applicability of these filters for both DFL and MDFL. Regardless of the filter solution, the results show that MDFL outperforms DFL in localization accuracy. For MDFL, the localization performance of the proposed filters is comparable. Apart from inaccuracies after initialization, both PMF and PF mostly achieve a localization performance below one meter. The localization performance therefore does not clearly indicate a preferred filtering solution. Decisive factors for the choice of the filter are complexity on the one hand and probability of divergence on the other. When considering large observation areas, the quadratic growth of complexity for the PMF can be crucial.

References

[1] S. Sand, A. Dammann, and C. Mensing, *Positioning in Wireless Communications Systems*. John Wiley & Sons, April 2014.

[2] MarketsandMarkets. (2020) Indoor location market – global forecast to 2025. [Online]. Available: https://www.marketsandmarkets.com/Market-Reports/indoor-location-market-989.html

[3] IEEE 802 LAN/MAN Standards Committee, "IEEE Standard for Information technology—Telecommunications and information exchange between systems Local and metropolitan area networks—Specific requirements - Part 11: Wireless LAN Medium Access Control (MAC) and Physical Layer (PHY) Specifications," *IEEE Std 802.11-2016 (Revision of IEEE Std 802.11-2012)*, pp. 1–3534, 2016.

[4] A. Kasher. (2020) WiFi sensing use cases. [Online]. Available: https://mentor.ieee.org/802.11/dcn/20/11-20-0936-00-SENS-usage-model-document.xlsx

[5] N. Patwari and J. Wilson, "RF sensor networks for device-free localization: Measurements, models, and algorithms," *Proceedings of the IEEE*, vol. 98, no. 11, pp. 1961–1973, Nov. 2010.

[6] Y. Guo, K. Huang, N. Jiang, X. Guo, Y. Li, and G. Wang, "An exponential-Rayleigh model for RSS-based device-free localization and tracking," *IEEE Transactions on Mobile Computing*, vol. 14, no. 3, pp. 484–494, Mar. 2015.

[7] O. J. Kaltiokallio, R. Hostettler, and N. Patwari, "A novel bayesian filter for RSS-based device-free localization and tracking," *IEEE Transactions on Mobile Computing*, 2019.

[8] M. Schmidhammer, M. Walter, C. Gentner, and S. Sand, "Physical modeling for device-free localization exploiting multipath propagation of mobile radio signals," in *Proc. 14th European Conference on Antennas and Propagation (EuCAP 2020)*, Apr. 2020.

[9] M. Schmidhammer, C. Gentner, S. Sand, and U. C. Fiebig, "Multipath-enhanced device-free localization in wideband wireless networks," *IEEE Antennas and Wireless Propagation Letters*, 2021, doi: 10.1109/LAWP.2021.3052438.

[10] A. F. Molisch, "Ultra-wide-band propagation channels," *Proceedings of the IEEE*, vol. 97, no. 2, pp. 353–371, Feb. 2009.

[11] P. Meissner, E. Leitinger, and K. Witrisal, "UWB for robust indoor tracking: Weighting of multipath components for efficient estimation," *IEEE Wireless Commun. Lett.*, vol. 3, no. 5, pp. 501–504, Oct. 2014.

[12] C. Gentner, T. Jost, W. Wang, S. Zhang, A. Dammann, and U. Fiebig, "Multipath assisted positioning with simultaneous localization and mapping," *IEEE Trans. Wireless Commun.*, vol. 15, no. 9, pp. 6104–6117, Sep. 2016.

[13] Y. Bar-Shalom, X. Li, and T. Kirubarajan, *Estimation with Applications to Tracking and Navigation: Theory, Algorithms and Software*. John Wiley & Sons, 2004.

[14] F. Gustafsson, "Particle filter theory and practice with positioning applications," *IEEE Aerospace and Electronic Systems Magazine*, vol. 25, no. 7, pp. 53–82, 2010.

[15] M. S. Arulampalam, S. Maskell, N. Gordon, and T. Clapp, "A tutorial on particle filters for online nonlinear/non-Gaussian Bayesian tracking," *IEEE Trans. Signal Process.*, vol. 50, no. 2, pp. 174–188, 2002.